Eur. Phys. J. B **32**, 457–469 (2003)
DOI: 10.1140/epjb/e2003-00127-2

THE EUROPEAN PHYSICAL JOURNAL B

How accurate can the determination of chiral indices of carbon nanotubes be?

An experimental investigation of chiral indices determination on DWNT by electron diffraction

M. Kociak[1,a], K. Hirahara[1], K. Suenaga[2], and S. Iijima[1,2]

[1] JST-ICORP Nanotubulites Project. Meijo university, Nagoya 468-8502, Japan
[2] National Institute of Advanced Industrial Science and Technology (AIST) Tsukuba, 305-8565, Japan

Received 23 December 2003
Published online 7 May 2003 –

Abstract. We present a general and systematic method for determining the chiral indices of carbon nanotubes. This method relies on the semi-quantitative analysis of experimental selected area diffraction pattern intensities, together with extensive comparison with kinematic theory. We show how to retrieve the chiral indices of single walled or multiwalled carbon nanotubes, even when their radii are large (up to approximately 40 Å). All theoretical and experimental sources of errors are discussed. By discussing the experimental case of a double-walled carbon nanotube, we show how it is possible to determine the chiral indices of each of its constituant tubes independently, by analyzing parts of the diffraction pattern where the contributions of these tubes do not interfere. Using the parts where all the contributions do interfere, we successfully crosschecked independently the preceding determination.

PACS. 61.14.Lj Convergent-beam electron diffraction, selected-area electron diffraction, nanodiffraction – 61.46.+w Nanoscale materials: clusters, nanoparticles, nanotubes, and nanocrystals – 81.07.De Nanotubes

1 Introduction

A Single Walled Carbon Nanotube (SWNT) can be described conveniently as a wrapped sheet of graphene. This wrapped structure was evidenced early on Multi Walled carbon nanotubes (MWNT) [1] and on SWNT [2] by selected area electron diffraction (SAED) experiments in a transmission electron microscope (TEM), where the diffraction pattern of an isolated nanotube can be obtained. The structure of a nanotube can be uniquely identified thanks to two parameters, (L, M), $-L/2 \leqslant M \leqslant L$, that are the coordinates of the wrapping vector in the honeycomb basis of the graphene sheet. Alternatively, it can be also uniquely described by the radius R of the nanotube and its helicity φ which is the angle enclosed between the circumference of the tube and the nearest zigzag chain. The relation between (R, φ) and (L, M) is given by

$$R = d_{cc}\frac{\sqrt{3(M^2 + L^2 + LM)}}{2\pi} \quad (1)$$

where d_{cc} is the distance between first neighbour atoms, and

$$\varphi = \arctan(\sqrt{3}M/(2L + M)). \quad (2)$$

The determination of the exact values of (L, M) or equivalently (R, φ) for an isolated SWNT, or for a small MultiWalled Nanotube or a rope of SWNT is of great importance, in particular for comparison with physical measurements. For example, it is well known that the band structure of SWNT has or does not have a gap at half-filling, depending on the exact value of (L, M) [3].

However, a complete structural determination is in practice a difficult task. An experimental technique with enough spatial resolution to study a unique (or a small number of) nanotube is required. This technique should also provide a high enough signal to noise ratio (SNR) for the structure of the nanotube to be determined, which means, in practice, enough SNR for the experimental data to be compared with relevant theoretical simulations. With this in mind, two types of techniques can be used. First, structural methods rely on the possibility of accessing R and φ either in real space (Scanning Tunnelling Microscopy [4,5] and phase reconstructed high resolution image (PRHR) [6]) or in reciprocal space (SAED [7]). A second type of determination (that can be used in conjunction with structural techniques) is based on spectroscopic measurements, either by Scanning Tunnelling Spectroscopy or by Raman spectroscopy. The Raman and STS spectra present well defined and sharp peaks related to Van-Hove singularities (VHS) in the electronic density

[a] *Present address:* Laboratoire de Physique des Solides, Université Paris-Sud, CNRS, Orsay 91405 France
e-mail: kociak@lps.u-psud.fr

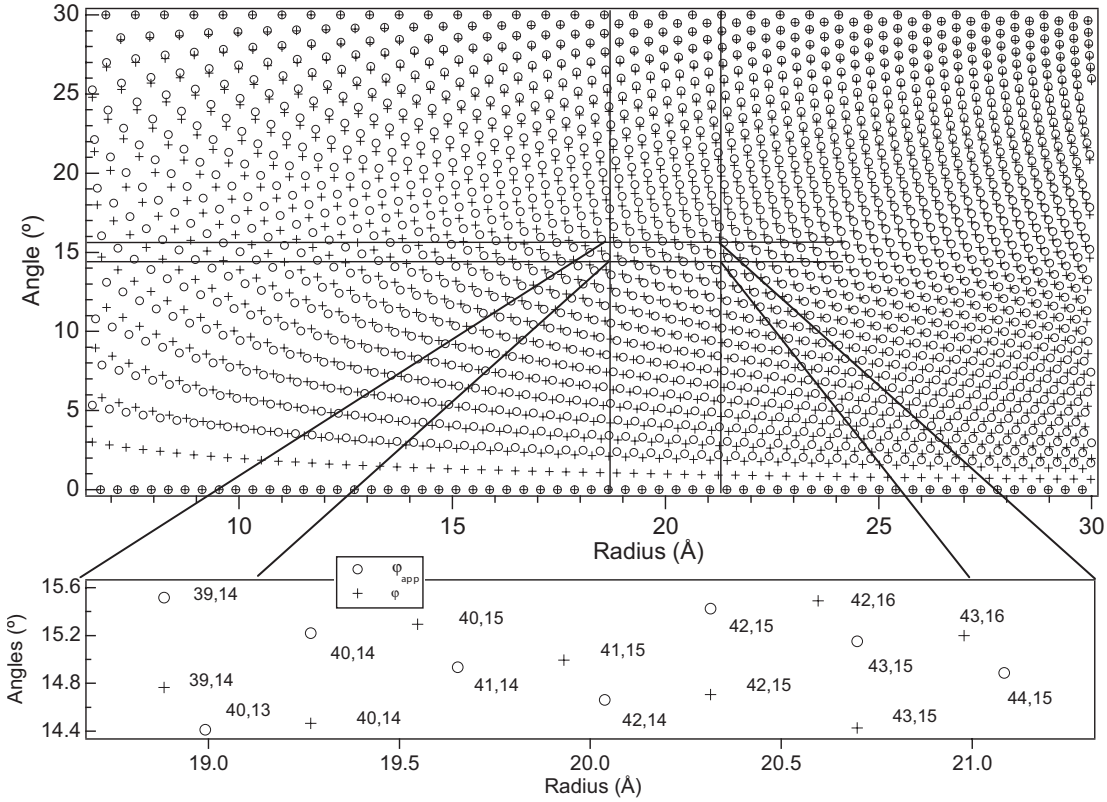

Fig. 1. Helicity φ and computed apparent helicity φ_{app} of carbon nanotubes as a function of their radius. φ_{app} is the helicity that would be deduced from a diffraction pattern from a naive point of view where the diffraction pattern of a SWNT is that of two rotated graphene sheets. Top: The difference between the two angles is huge, but decreases with increasing radius and helicity value. The lines define typical experimental errors when measuring radius and helicity on a typical nanotube of radius $R \approx 20$ Å and $\varphi_{app} \approx 15°$. Bottom: magnification of the error area. It is worth noting that, unless taking into account the difference between φ and φ_{app}, only half of the possible solutions would be retrieved from measurement.

of states of the nanotube. The positions of the VHS are highly dependent on the exact value of (L, M). Given a model band-structure – usually obtained by the tight binding approximation –, simulated spectral singularities can then be fitted with the experimental ones, and the (L, M) indices can be deduced [9,10]. Such fitting rely on at least one parameter, namely the hopping integral γ_0 [9,10]. It is worth noting that no agreement has been found up to now between the two techniques on the value of γ_0, that ranges between 2.5 eV and 2.9 eV.

The intrinsic difficulty in determining the chiral indices from experimental data on an arbitrary nanotube can be understood as follows. For structural techniques, the value of the radius is usually known to within $\pm 10\%$, and the value of φ is generally known to within $\pm 1°$ [4,5,7,8,10], although this value can be reduced to $\pm 0.2°$ under favourable conditions in diffraction experiments [11,12]. It is worth noting that due to the curvature of the SWNT, the helicity cannot be measured directly. Instead, an apparent helicity φ_{app} can be defined (see Sect. 3 for a precise theoretical and experimental definition in the case of SAED). This fact was first noticed by Qin for the SAED [7] and described by Meunier *et al.* for the STM [8]. Roughly speaking, the hexagons forming the real space honeycomb lattice appear distorted in STM images, or equivalently, in the reciprocal space, appear in SAED as a superposition of two lattices which are not perfectly triangular. Top of Figure 1 displays the computed helicity and apparent helicity values as a function of the radius, in the case of SAED. See Section 3.1 for the detail in computing φ_{app}. It is striking that the difference between both angles values can be huge, and should be taken into account prior to any quantitative analysis. As an example, for hypothetical realistic experimental values ($R = 20 \pm 2$ nm, $\varphi_{app} = 15 \pm 0.6°$), emphasized at the bottom of Figure 1, several solutions are possible. This remains true in the general case, unless having small (of the order of 1nm) tube diameters (see [7] for an SAED example or [4] for an STM one), or narrower uncertainties thanks to high SNR [11,12]. Indeed, STM results must usually be refined by STS measurements [8,9]. However, because STM/STS is a surface technique, it is basically not extendable to MWNT or ropes. Resonant confocal micro-Raman spectroscopy was shown to successfully determine (L, M) [10] of individual SWNT without *a priori* structural knowledge (except for the first estimation of the diameter by Atomic Force Microscopy). This technique is however restricted to small diameters [10]

and, to our knowledge, was not used on individual multi-walled nanotubes (MWNT).

On the contrary, SAED in a Transmission Electron Microscope (TEM) is not restricted to SWNT. For example, Amelinckx *et al.* [13] studied in detail the apparent helicities of MWNT and ropes. More recently, Colomer and coworkers [14] concentrated their study on ropes with unique helicity, for which the apparent helicity can be unambiguously measured. In a previous work [11], we also used SAED to determine the chiral indices of both nanotubes inside a DWNT. This determination was compared to an *in situ* transport experiment on the same DWNT in a TEM. The successful chiral indices determination proved the impressive accuracy of the SAED for resolving chiral indices of arbitrary large radius (around 30 Å) MWNT. In this previous work, we extended the original systematic procedure of Qin [7], from SWNT to DWNT. Qin's procedure allows the retrieval of the helicity from the apparent helicity measurement, and, knowing the diameter value, to determine the chiral indices in favourable cases. In Qin's procedure, the radius of a SWNT was measured with High-resolution imaging (HR), although in our previous study we used the diffraction pattern itself to measure the radii of a DWNT. Nevertheless, in our previous work [11], the discussed ambiguities on the exact value of the chiral indices still remained for most of the investigated structures. This led us to find a more powerful method to extract chiral indices from the diffraction pattern.

The diffraction pattern intensity of a nanotube has a discrete periodicity along the tube axis, while it oscillates in the perpendicular direction. While the very well defined discrete periodicity depends on the exact value of (L, M), the (pseudo) periods of the oscillation are related to the diameter(s) of the nanotube(s) under consideration, as well as their mutual structural arrangement. It is therefore obvious that a huge improvement in the structural determination accuracy of a SWNT, a MWNT or a rope of SWNT can be gained by analysing these features. To study the structural order and disorder in ropes of SWNT, Henrard *et al.* [15] and Colomer *et al.* [14] used the central oscillations of the diffraction pattern. On the other hand, Amelinckx *et al.* [13] used the modification of the periodicity of the diffraction pattern when tilting the nanotube to retrieve the tilting angle. So far, no experimental work has analysed the fine structures of the whole diffraction pattern, nor were these fine structures used to determine the chiral indices.

We will show that a determination of chiral indices based on SAED measurement of radius and apparent helicity can be refined by semi-quantitative analysis of the diffraction pattern. This analysis gives unambiguously the chiral indices. It relies on an extensive comparison of experimental data with simulation made using the kinematic diffraction theory developed by Lambin and Lucas [17]. The determination of the chiral indices can then be deduced for an arbitrary large nanotube, nested or not. We give the general procedure, illustrated by an example, of the determination by SAED of the chiral indices of the two tubes constituting a DWNT. We will show how it is possible to extract this information either independently for the two nanotubes, or in parallel. All experimental and theoretical uncertainties will be discussed in detail. We will discuss the fact that this method does not rely on any fitting parameter and should apply to tube of arbitrary size. Most of this analysis could apply to any kind of nanotube (SWNT, MWNT or ropes) and could be easily extended to nanotubes made up of different chemical species.

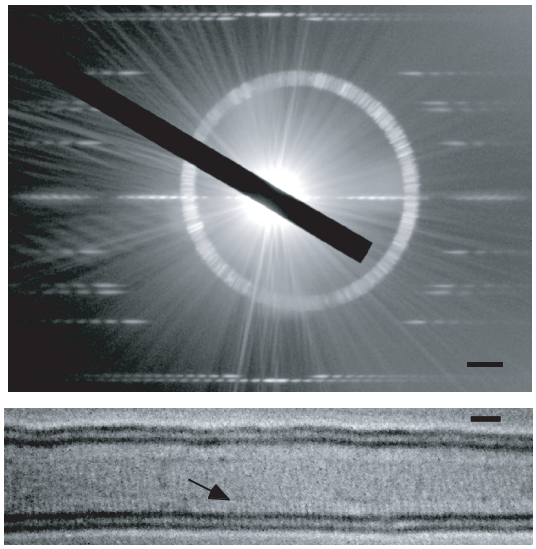

Fig. 2. Diffraction pattern and image of the same DWNT. Top. The diffraction pattern was taken on Imaging Plates, with an acquisition time of 180 s, a camera length of 80 cm and a selected aperture of 500 nm. The scale bar is 100 pixels. One clearly distinguishes the layered distribution of the diffracted intensity, as well as its oscillating behaviour. The black rectangle is the beam stopper, and the iris-like feature an artefact. The Selection Aperture was not centred on the tube, in order to avoid diffraction by nanoparticles in the vicinity. Bottom: Image of the same DWNT. The black fringes are related to the presence of the two walls. Notice the fringes (indicated by an arrow) perpendicular to the tube axis, which are related to the zigzag chains. The scale bar is approximatively 1 nm.

2 Experimental results

2.1 Experimental conditions

Figure 2 presents both the diffraction pattern and the image of a DWNT produced by arc-discharge [11]. The experiment was performed in a JEOL 2010 F, fitted with a Field Emission Gun (FEG), working at an acceleration voltage of 117 keV. Working below 120 keV was found to decrease the probability for the nanotube to be damaged by knockout atom ejection. The DWNT was suspended freely in the vacuum, supported on both sides by an amorphous carbon film. The diffracting geometry is schematized in Figure 3. An incoming electron beam parallel to the X axis is diffracted by a DWNT, and forms a

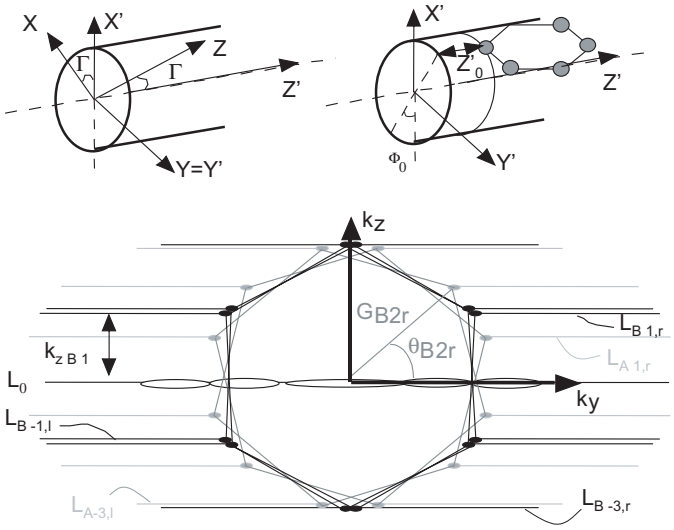

Fig. 3. Scheme and notations. Top: Diffraction geometry (only one tube is schematized here). The reference XYZ refers to the TEM, the diffraction plane YZ being perpendicular to the optical axis X. The tube axis is parallel to Z', and makes an angle Γ with Z. In the reference frame of the nanotube, an arbitrary atom (grey dot) is translated by Z'_0 and rotated around the circumference by an angle Φ_0. Bottom: Scheme of the diffraction pattern of DWNT presented in Figure 2. Except for the central line, each line can be attributed uniquely to one or the other of the two tubes constituting the DWNT. The first maxima (two per line) of the lines are helpful to quickly assign each line to a tube. They form one set of two pseudo-hexagons symmetric with respect to k_Z per tube. Grey lines and hexagons are then attributed to a first tube called tube "A", and black ones to the (nearly zigzag) tube "B". Different quantities can be defined. In the subscripts, "A or B" stands for the type of tube, the number following denote the index of the layer for the given tube, and "r" or "l" stands for "right" and "left".

diffraction pattern in the YZ plane. The tube axis, parallel to Z', is enclosing an angle Γ with Z. Γ will be referred later as the tilting angle. Several diffraction patterns were acquired with different acquisition times (from 4 s to 180 s) on Imaging Plates (IP) for a camera length value of 80 cm. We used the smallest available selection area aperture (equivalent to 0.5 μm in the object plane), to avoid diffraction by neighbouring catalyst or graphitic particles. We set the condenser illumination in order to obtain the most nearly parallel incoming beam on the DWNT, and we then focused the intermediate lens so as to obtain the finer details on the diffraction pattern. This ensures an optimal sharpness of the diffraction features, at the expense of decreasing the available signal. Because for this work we were primarily interested in the fine structures of the diffraction pattern, we used IP in order to obtain a signal proportional to the diffracted intensity and with a high dynamic range. However, using standard films increases the sensitivity with the drawback of losing linearity. Note that experiments on smaller nanotubes with IP and a parallel incoming beam give a very poor signal to noise ratio, making the retrieval of the chiral indices much harder. In this case, a balance between increasing uncertainties over the diameter and helicity measurements on one hand, and the increase of signal on the other should be found when using a non-parallel beam and standard films [16]. The high-resolution image was then acquired on a CCD Gatan camera, mostly in order to check that the tube was not damaged. Successive diffraction patterns were acquired over an elapsed time of more than 15 mn without any noticeable electron beam induced damages, either on the diffraction patterns or on the images.

2.2 Image

On the image (bottom of Fig. 2), one clearly distinguishes two pairs of black fringes, reminiscent of the projection of the two walls of the DWNT [1]. On the bottom of the image, one can notice a series of parallel fringes perpendicular to the tube axis. This is the imaging of the zigzag chains on one side of the DWNT [6], which occurs when a nanotube is tilted so that the tilt angle is nearly equal to the helicity, namely $\Gamma \sim \varphi$. Note that in this case, the fringes are imaged only on one side of the tube. It is worth noting that with only a single HR image and without any image simulation, it is impossible to determine the chiral indices. It is even impossible to tell which of the two shells is responsible for the appearance of the zigzag fringes.

2.3 Qualitative description of the diffraction pattern

The top of Figure 2 displays the diffraction pattern of the same DWNT. A scheme of the diffraction pattern is shown in Figure 3. Note that the iris-like feature, as well as the radial stray lines, are artifacts related to the condenser aperture.

As outlined in Figures 3, 4 sets of 6 broad spots, forming 4 pseudo hexagons, 2 by 2 symmetric with respect to the k_z axis can be immediately identified. A heuristic and qualitative point of view allows us to attribute each pair of hexagons to the intensity diffracted by each unique single walled nanotube forming the DWNT (see for example [13] for a review of the different models for nanotube diffraction). Indeed, let us assume that only the parts of the tubes that are perpendicular to the incoming electron beam are likely to diffract. For each tube, we can approximate these two parts by two graphene sheets, rotated with respect to each other by an angle 2φ. Thus, the diffraction pattern for one nanotube would then be constituted by the superposition of the diffraction patterns of two rotated graphene sheets. The resulting first spots of such a diffraction pattern are then forming two hexagons, rotated by an angle 2φ. However, due to the finite curvature of a nanotube, this is only very qualitatively true. First, the "spots" are broad, which implies to clearly define where the characteristic angles are measured. Secondly, whatever the definition chosen for measuring an angle on one of these broad spots, the measure of this angle will be different from the helicity [7]. For example, without curvature, $\varphi = \theta_3 = 30 - \theta_1$, which is clearly not the case for

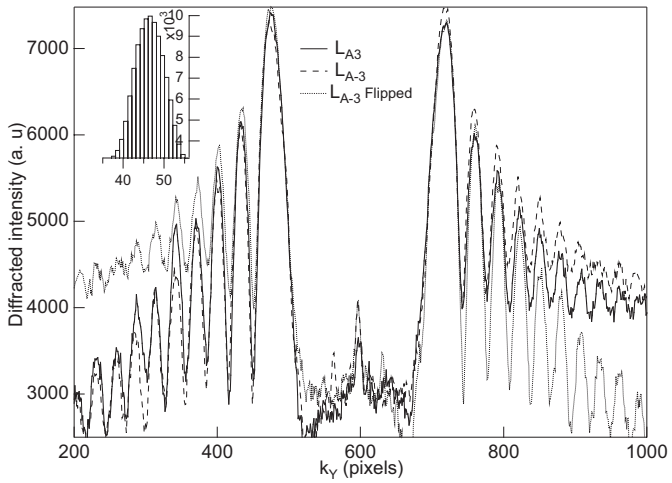

Fig. 4. Principal features of the diffraction pattern. Main panel: An intensity profile has been extracted from two symmetric layer-lines, denoted L_{A3} and L_{A-3} (see Fig. 3 for definitions). Integration width is 11 pixels. The diffraction pattern is almost symmetric with respect to the k_Y axis. L_{A-3} as also been drawn after a mirror symmetry has been applied with respect to the k_Z axis, in order to emphasize the symmetry with respect to this axis. The resulting curve is labelled L_{A-3} *Flipped*. The maxima are symmetric, but the background is not. Inset: Intensity profile perpendicular to L_{A3}, with an integration width of 7 pixels. The position of the maximum, clearly above the noise, is independent of the integration width, emphasizing the experimental accuracy available in determining the layer-line positions.

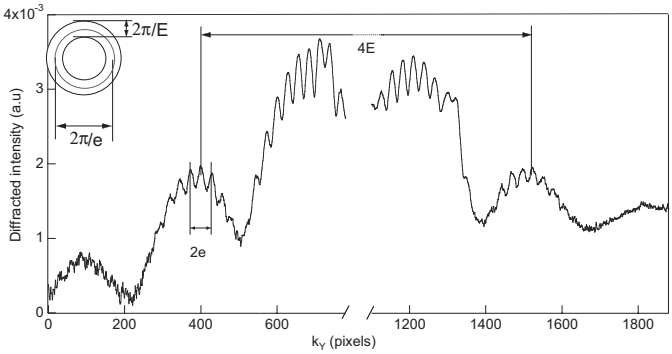

Fig. 5. Intensity profile of the equatorial line. The central spot has been skipped for clarity. As for the other layers, one notices a small asymmetry of the background. "E", 2π times the inverse of half the difference of the tube diameters and "e", 2π the inverse of the mean tube diameter (see inset for real-space representation of these quantities) can be extracted.

real nanotubes (see the comparison of $\varphi_{app} = 30 - \theta_1$ with φ in Fig. 1). Nevertheless, such a simple model allows us to have a first idea of the contribution of the two tubes, arbitrarily noted A and B from now on.

An accurate description of the diffraction pattern can be done as follows [7,13,17]. The intensity is distributed on a discrete set of lines parallel to k_Y and symmetric with respect to the central line. This line, that we will call hereafter the equatorial line, is noted L_0 in Figure 3. This comes from the fact that a nanotube has a translational periodicity along its axis, and none in the perpendicular direction. Following [17], we will call these lines "layer-lines". As we have seen, except for the equatorial line, each layer-line intensity depends upon one and only one of the two tubes constituting the DWNT, except if their periodicities are commensurable. The layer-lines will then be labelled $L_{(A\ or\ B),\pm i,(r\ or\ l)}$. *A or B* refers to the corresponding nanotube, $\pm i$ to the position with respect to the equatorial line, and *r or l* refers to the right or left of the diffraction pattern, when needed. In Figure 3, the position of these lines with respect to the equatorial one are noted $k_{z,i}$. Similarly, the distance from the 000^* spot to a given maximum in intensity will be labelled $G_{(A\ or\ B),\pm i,(r\ or\ l)}$, and the corresponding angle, $\theta_{(A\ or\ B),\pm i,(r\ or\ l)}$. The central line oscillates with two periods, while the others display two broad maxima, symmetric with respect to k_Z, and followed by weaker oscillations, as seen directly on the diffraction pattern of Figure 2.

In order to quantitatively analyse the diffracted intensities, we extracted intensity profiles along a given line, using the profile tools of Digital Micrograph from GATAN inc. For a given pixel along the line, the intensity is averaged over a certain width perpendicular to the profile line. The width is chosen as to maximise the signal to noise ratio, and is usually in the range between 4 to 10 pixels. This is exemplified in Figures 4 and 5, in which the intensities along the equatorial line and two symmetric lines are respectively displayed. Thanks to the use of IP, the intensity in not saturated for the equatorial line, and the dynamic range is good enough to measure both the equatorial line and the other layers. Note the high number of visible oscillations on layer-lines $L_{\pm 3}$ for both tubes. The number of oscillations is less on the other layer-lines, typically 3 or 4. The symmetry with respect to k_Z involves not only the position of the intensity maxima, but also their value, apart from an asymmetric background (seen on every line). This asymmetric background results from the fact that the DWNT was slightly misaligned with respect to the SA aperture in order to avoid diffraction from neighbouring particles. The symmetry of the intensities on two layer-lines symmetric with respect to the k_Y axis is emphasized in Figure 4 (see the comparison of curves "L_{A3}" and "L_{A-3}").

As we will see in the next paragraph, $k_{z,i}$, G_i and θ_i (see Fig. 3), and e and E (see Fig. 5) will be used to deduce the structure of the nanotubes. The angles θ_i will be related to the helicity of each tubes, and e and E to the inverse of the mean diameters and the intertube distance. It is then important to comment on the accuracy in measuring these quantities on the diffraction pattern, prior to any assumptions.

The displayed area of the IP in Figure 2 is about 2000 pixels in width and in height. The positions of the layers (the quantities "$k_{z,i}$" in Fig. 3) are very well defined. The inset of Figure 4 displays the diffracted intensity perpendicular to a line. Though the Full Half Width of

this profile is of the order of 10 pixels, the position of its maximum does not depend either on the averaging width, or on the precise position of the profile line, provided it is perpendicular to the intensity layer-line under consideration. This means that the measure of $k_{z,i}$ can be performed with an accuracy of ± 1 pixel, which represents a precision of $\pm 2/1000$ for $L_{\pm 3}$. Among all the measured distances, it is by far the most precise. For a given layer-line i, let $k_{ymax,i}$ be the position of the first maximum. We define then,

$$G_i = \sqrt{k_{ymax,i}^2 + k_{z,i}^2} \tag{3}$$

and

$$\theta_i = \arctan(k_{z,i}/k_{ymax,i}). \tag{4}$$

The accuracy in measuring these two quantities will be limited mainly by the accuracy in determining $k_{ymax,i}$. An accuracy of ± 5 pixels on $k_{ymax,i}$ is a pessimistic precision that can be easily achieved. Then, the accuracy of G_i will be on the same order in pixels, and on the order of $\pm 1\%$. Note that the larger $k_{z,i}/k_{ymax,i}$, the smaller is the error on G_i. This means that it is better to measure a distance on layers $L_{\pm 3}$ than on layers $L_{\pm 1}$. The corresponding errors in θ_i are typically $\pm 0.3^\circ$ to $\pm 0.6^\circ$. The accuracy of θ_i is increased when measuring angles for which $k_{ymax,i}$ is large as compared to $k_{z,i}$. This means that, contrary to the distance determination, the angle determination is better on layers $L_{\pm 1}$. Errors made in determining e arise mainly from intrinsic noise during acquisition. It can be decreased down to ± 1.25 pixels by averaging over three maxima. This represents a relative error of $\pm 5\%$, which is the worst accuracy of all the important measured quantities. Finally, the error in determining E comes mainly from the detection of the maxima, rapidly oscillating at the period e, in between which this quantity is measured. By allowing an error of $\pm e/2$ on the position of these maxima, and measuring directly $4E$ (see Fig. 5), the errors is $\pm e/4$, which represents only around $\pm 2\%$ of E.

3 Analysis

3.1 Theory

In order to fully interpret the diffraction pattern, we will make use of the theory developed by Lambin and coworkers [13,17] for the general case of a SWNT, a MWNT or a rope of tubes, that we will apply specifically to the case of a DWNT. Note that a kinematic theory is fully justified for such thin objects like the DWNT under consideration. We will use the notations found in [17]. It is convenient to describe the nanotube in a slightly different manner from that in the introduction, in order to include explicitly the handness ($\sigma = \pm 1$) of the nanotube. In particular, a SWNT with $M < 0$ is equivalent to the one with $(L + M, -M)$ but with the opposite handness. Any nanotube can then be described easily from the knowledge of (L, M) and σ. Let C be the circumference of the nanotube, and T the translational vector of the SWNT [18]. We will first describe the reciprocal space of a SWNT and then that of a DWNT. Because in electron diffraction the Ewald sphere is almost flat, the salient properties of the diffraction pattern can be deduced from the reciprocal space in a framework where the diffraction pattern is a simple plane containing k'_z [7].

Let $\boldsymbol{k}$ be the wave-vector transfer in the geometry described in Figure 3, $\boldsymbol{k}_\perp$ the projection of $\boldsymbol{k}$ in the $X'Y'$ plane and $\phi_{\boldsymbol{k}}$ the azimuth angle of $\boldsymbol{k}_\perp$ in the $X'Y'$ plane. Then, for a SWNT (L, M) of given handness σ, the diffracted amplitude $A_{ss}(\boldsymbol{k})$ reads [17]:

$$A_{ss}(\boldsymbol{k}) = \frac{4\pi C}{3\sqrt{3}d_{cc}} \sum_{l=-\infty}^{+\infty} F_l(\boldsymbol{k})\delta[k_{z'} - (2\pi/T)l] \tag{5}$$

with the diffracted amplitude on a layer-line l reading:

$$\begin{aligned} F_l(\boldsymbol{k}) &= \exp(\mathrm{i}2\pi z'_0 l/T) \\ &\times \sum_{m,s=-\infty}^{+\infty} J_{sL'-mM'}(k_\perp R) \exp \mathrm{i}\Big\{(sL' - mM') \\ &\times \left[(\phi_k - \phi'_0)\sigma + \frac{\pi}{2}\right]\Big\} f_C(\boldsymbol{k})\{1 + \exp \mathrm{i}2\pi[(s+2m)/3]\} \\ &\times \delta\left(l, \frac{s(L'-2M')}{N} + \frac{m(L'+M')}{N}\right) \end{aligned} \tag{6}$$

with $L' = L + 1/2(1-\sigma)|M|$ and $M' = \sigma|M|$. z'_0 and ϕ'_0 are respectively the shift distance along the Z' axis and the rotation angle around this axis for an arbitrary carbon atom of the nanotube (see Fig. 3). $J_n(x)$ is the first Bessel function of order n and $f_C(\boldsymbol{k})$ the atomic form factor of carbon.

For a DWNT, the diffracted amplitude will be just the sum of that of the two constituting tubes. Let us first describe the reciprocal space of a SWNT. The amplitude is non zero only on successive planes of equation $k_{z'} = (2\pi/T)l$ where the allowed layers l for a given tube are determined by the extinction rules (see [7] for a geometrical description of them):

$$l = \frac{s(L'-2M')}{N} + \frac{m(L'+M')}{N}. \tag{7}$$

For a given l and for a given direction of the $\boldsymbol{k}_\perp$ vector (*e.g.* for a fixed value of ϕ_k) the amplitude will be proportional to a sum of Bessel functions of order $n = sL' - mM'$, the values of which are determined through equation (7), weighted by a phase factor that mainly depends on $(\phi_k - \phi'_0)\sigma$. Note that for $l = 0$, $n = 0$ is always a trivial solution of equation (7), while in the general case, n depends on L, M (but not on the handness) in an intricate way. Forgetting for clarity the monotonically decreasing behaviour of the atomic form factor, we can concentrate on the behaviour of the Bessel functions. The behaviour of a $J_n(k_\perp R)$ function can be schematized as follows: it has a first maximum at $k_\perp \sim n/R$, followed by decreasing pseudo-oscillations of period $\approx 2\pi/R$. This means that a given nth order Bessel function will contribute only from $k_\perp \gtrsim n/R$. As a matter of fact, except for the highly symmetric case of zigzag and armchair

tubes, there's only one Bessel function contributing to a given layer l, at least for reciprocal space distances up to $k_\perp \sim 2\times 2\pi/d_{zz}$, where d_{zz} is the distance between zigzag chains. One practical consequence is that, for a SWNT, all the phase factors in equation (5) factorize, and so the diffracted intensity on a given layer l, $I_{ss,l}(\boldsymbol{k}) = |A_{ss,l}(\boldsymbol{k})|^2$ takes a very simple form:

$$I_{ss,l}(\boldsymbol{k}) \propto |J_n(k_\perp R) f_C(\boldsymbol{k})|^2. \quad (8)$$

This means that all information on the atoms absolute positions (the knowledge of z'_0 and ϕ'_0) and the handness is not available in this case. On the contrary, the oscillation pseudo-period will give us extra information on the radius of the nanotube.

The symmetry of the reciprocal space can be easily deduced: making the inversion $k_{z'} \to -k_{z'}$, *i.e.* $l \to -l$, implies from equation (7) $(s,m) \to (-s,-m)$ and then $n \to -n$. Since $J_n(k_\perp R) = J_{-n}(k_\perp R)$, this means that the reciprocal space of a SWNT is symmetric with respect to the plane (X,Y). Also, because $J_n(k_\perp R) = J_n(-k_\perp R)$, the reciprocal space is also symmetric with respect to the $k_x = k_y = 0$ line. Although we derived these two symmetries from (8), they remain true in the general case [13]. Also, for a chiral tube, the reciprocal space is invariant by rotation around k_z [13]. Taking into account the curvature of the Ewald sphere does not change substantially this analysis for chiral tubes [13], but the symmetry with respect to the central line will be slightly broken in case where the nanotube is tilted, the effects becoming noticeable typically for tilt angles larger than 10°. This is in agreement with the symmetry observed on the experimental diffraction pattern (Fig. 2) and the intensity on a layer-line, Figures 4 and 5.

For a DWNT nanotube, made up of a tube A and tube B, the description of the reciprocal space can be divided in two parts. First, for $k_{z'} \neq 0$, except if tube A and B are commensurate tubes, $l_A/T_A \neq l_B/T_B$ for any l_A, l_B. Then, tube A and B do not contribute to the same layers, and the intensity takes the simple form of equation (8), with n depending on the layer l under consideration and R being R_A or R_B. Secondly, when $k_z = 0$, the solution $l = 0$ is valid for both tubes. The diffracted amplitude A_{dw} will be the sum of that of tube A and B. Assuming that only the Bessel function of order $n = 0$ is contributing to that layer, the diffracted intensity reads:

$$I_{dw,0}(\boldsymbol{k}) \propto |C_A J_0(k_\perp R_A) + C_B J_0(k_\perp R_A)|^2 \times \left(\frac{8\pi}{3\sqrt{3}d_{cc}} f_C(\boldsymbol{k})\right)^2. \quad (9)$$

In this case also, although contribution of both nanotubes interfere, all effects of the relative shift along the tubes axis, namely $(z'_{0,A}, z'_{0,B})$, relative rotation $(\phi'_{0,A}, \phi'_{0,B})$ and handness have disappeared as in the case of equation (8). A useful limit can be found by using the asymptotic formula for the Bessel function [13], for large enough $k_\perp$. "Large enough" means reciprocal distances larger than $\frac{2\pi}{d_{zz}}$ [13], *i.e.* of the order of G. In this case, we can expand the formula equation (9) for large values of the wave vector and in power of the adimensional parameter $\delta R/R$:

$$I_{dw,0}(\boldsymbol{k}) \sim f_C^2(\boldsymbol{k}) \times \left\{ \left(\cos^2\left(k_\perp \overline{R} - \frac{\pi}{4}\right)\cos^2(k_\perp \delta R) + \frac{1}{4}\frac{\delta R}{\overline{R}} \sin\left(2k_\perp \overline{R} - \frac{\pi}{2}\right)\sin(2k_\perp \delta R) + o\left(\frac{\delta R^2}{\overline{R}^2}\right)\right)\right\}. \quad (10)$$

Here, $\delta R = \frac{|R_A - R_B|}{2}$ and $\overline{R} = \frac{R_A + R_B}{2}$.

As previously noted in [11], the first part of this expression is similar to that extracted from a simple model where the main contribution to the equatorial line comes from the Young-slit-like diffraction by the generator lines of the two tubes. The intensity along the equatorial line oscillates with a period of $e = 2\pi/2\overline{R}$, within an oscillatory envelope of period $E = 2\pi/2\delta R$. This appears on the experimental diffraction pattern (Fig. 2) as well as in the intensity profile of Figure 5. Note that the second part of the right term of equation (10), of order $\frac{\delta R}{\overline{R}}$, also contains a multiplication of two functions with the same periods as the first one.

Let us finish the theoretical description of the diffracted pattern by examining the effect of the tilting angle Γ. It will increase the distances $k_{z,i}$ of the layer-lines with respect to the equatorial line (see Fig. 3):

$$k_{z,i}(\Gamma) = k_{z,i}(\Gamma = 0)/\cos(\Gamma). \quad (11)$$

Also, as already discussed, due to the finite curvature of the Ewald sphere, a tilting angle will change slightly the diffracted intensity along a layer-line, the effect being possibly assymetric with respect to the central line.

3.2 General procedure

We come now to our main concern: given an experimental diffraction pattern with its experimental uncertainties, how can we determine the chiral indices? And what is the level of confidence in this determination?

We will propose a general method to tackle these questions. First of all, we will discuss the critical questions of the calibration of the diffraction pattern, identifying the measured quantities depending or not on it, and the additional uncertainties arising from badly calibrated diffraction patterns (Sect. 3.2.1). Because the contribution of each tube inside a DWNT generally decouples except for L_0, we will be able to determine independently their chiral indices. With this objective, we will first determine the possible values for the diameters and the corresponding uncertainties in Section 3.2.2. Similarly, we will determine the apparent helicities in Section 3.2.3. In Section 3.2.4, using the database in Figure 1, we will determine for each tube independently the possible chiral indices, given the diameter, helicity and related uncertainties. Then, among all the theoretical solutions, we will use extra information, namely the comparison of the experimental layer-line positions $k_{z,i}$ to their theoretical counterparts, and the fit of the layer-lines intensity with their theoretical counterpart to discard all but one solution for each tube independently. Gathering the solution for tube A and tube B, it

would be then interesting to confirm this unique solution $(L_A, M_A), (L_B, M_B)$ by an independent measurement. On the equatorial line the contribution of the two tubes interfere. We will show in Section 3.2.5 how it is possible to determine directly the chiral indices of both tubes at the same time, and that only one solution fits the experimental data. This solution will prove to be exactly the same solution as deduced from the preceding analysis.

3.2.1 Calibration

As explained before, the calibration of the diffraction pattern (expressed in units of rad Å^{-1}/pixel) depends on the experimental settings for each experiment. It is in principle possible to achieve a calibration with a precision better than 1% using a known standard (polycrystalline gold for example). This requires recording the diffraction pattern of the standard under exactly the same conditions as the nanotube of interest. Although this can be done in a dedicated experiment, it is beyond the scope of many experiments. For example, during *in situ* transport measurements, it is unlikely to have an available standard near the nanotube of interest. Also, the nanotube can be highly defocused with respect to this standard.

Moreover, given an absolute calibration, the determination of the diameters (see Sect. 3.2.2) along a given layer-line (Sect. 3.2.4) should depend on the exact value of the carbon-carbon distance d_{CC}, that, depending on the authors, ranges between 1.42 and 1.44 Å [15,18]. It is then obvious that a standard calibration procedure, independent of d_{cc} should be useful.

First, let us note that the measure of the angles θ does not depend on the calibration. Also, for a given nanotube, the layer-line ratios $k_{z,i}/k_{z,j}$ do not depend on the calibration. Nevertheless, the measured θ do depend on the tilting angle Γ, which is not the case for the layer-line positions ratii. Noticing that the measurement error on k_z is of the order of 0.1%, $k_{z,i}/k_{z,j}$ should be the most sensitive experimental quantity that can be compared to the theoretical one.

Second, we can accurately calibrate the diffraction pattern, given the measure, on the same diffraction pattern, of a distance theoretically proportional to $1/d_{cc}$. Indeed, the intensity along a layer line (see Eq. (8)) is essentially dependent on the adimensional parameter $k_\perp R$ ($f_C(\boldsymbol{k})$ is a slowly varying function). Then, as $k_\perp \sim 1/d_{cc}$, we can easily measure R/d_{cc} which does not depend either on d_{cc}, or on the exact value of the acceleration voltage. For the sake of simplicity, all distances (real-space and reciprocal-space) will be given assuming $d_{cc} = 1.44$ Å, but it should be kept in mind that only adimensional parameters like

$$R/d_{cc} = \sqrt{3(L^2 + M^2 + LM)}/2\pi \qquad (12)$$

are really measured.

Using G (see Sect. 2.3) as a calibration length is a good starting point, because in the naive model of the two diffracted graphene sheets, $G = \frac{2\pi}{d_{zz}}$. However, three kinds of errors can arise when calibrating the diffraction pattern with G. First, the intrinsic measurement error on G (the error in pixels) is of the order of $\pm 1\%$ (see Sect. 2.3). This error cannot be decreased, and for a better calibration we could use other characteristic distances, like $k_{z,i}$ (see Sect. 3.2.4). Secondly, due to the curvature effect, G should be reexpressed

$$G = \tau(L, M, \mathrm{i}) \times 2\pi/d_{zz}. \qquad (13)$$

The factor τ, which can be as high as 1.05, depends on the particular layer on which the measurement is done, and also on the chiral indices of the nanotube. However, τ is theoretically known, and this error can be discarded in a second step (see Sect. 3.2.4). Finally, G depends on the tilting angle, generally unknown. Because the nanotube lies horizontally on the carbon grid, we guessed that $\Gamma \lesssim 6°$. This induces an additional error less than $1/\cos(\Gamma = 6°) \sim 1\%$. For higher tilt values, the influence increases quickly. For example, $10° < \Gamma < 30°$ induce a relative change of the calibration between 1.5% and 15%. In this case, an iterative procedure should be used [7].

3.2.2 Measurement of diameters

As explicitly given in equation (10), the mean diameter and inter-radius distance can be deduced from the measurement of the quantity e and E (see Fig. 5). It is important to note that these quantities must be measured approximately at wave vectors superior or equals to $2\pi/d_{zz}$, in order for equation (10) to hold. The guess calibration is done assuming $G_{B3} = 2\pi/d_{zz}$. Taking into account the intrinsic errors on the measurement of e and E discussed in Section 2.3, the intrinsic error on G_{B3}, and the estimated error due to the curvature effect (in this case, $\pm 1\%$) and the tilt (in this case, $\pm 1\%$), we find: $\overline{D} = 37.89 \pm 3.5$ Å and $\delta D = 3.79 \pm 0.19$ Å. We can then deduce the inner and outer diameters. Let's call D^- and D^+ the inner and outer diameters. $D^- = 34.10 \pm 4.2$ Å and $D^- = 41.68 \pm 4.2$ Å. It is worth noting that the very poor uncertainties (around 12%) on both diameters are clearly overestimated. First, the uncertainty on the calibration length can be decreased, by using a less noisy quantity (like $k_{z,i}$) and by recalibrating this length on a known theoretical length (see Sect. 3.2.4). Second, the experiment gives directly δD, within errors. Thus, all combinations such as $(D^+ - D^-)/2 \neq \delta D$ (within errors) would be filtered out. However, for the sake of proving the amazing resolution of the diffraction analysis, we will begin with such huge uncertainties.

3.2.3 Measurement of helicity

Apparent helicities are measured on the θ_1 angles ($\varphi_{app} = 30 - \theta_1$), because, compared to θ_2 and θ_3, they are less sensitive to both the uncertainties due to difficulties in measuring the maxima on a given layer-line and to the tilting angle Γ. An uncertainty of $\pm 0.3°$ due to the unknown tilting angle adds to the intrinsic one discussed in

Section 2, giving a total uncertainty of $\pm 0.6°$. These values can be refined, especially when the maxima are better defined, to a value of about $\pm 0.2°$. However, still to prove the efficiency of the present methods, we will not try to refine these values. The experimental values are then $\theta_{A,1} = 16.34 \pm 0.65°$ ($\varphi_{app,A,1} = 13.66 \pm 0.65°$) and $\theta_{B,1} = 27.67 \pm 0.65°$ ($\varphi_{app,B,1} = 2.33 \pm 0.65°$).

3.2.4 Determination of possible solutions

For a given θ_1 (or equivalently φ_{app}), there are two possible diameter ranges, namely $D^+ \pm$ uncertainties and $D^- \pm$ uncertainties. We computed all possible couples of diameters and θ_1 for $1 \leqslant L \leqslant 100$ and $0 \leqslant M \leqslant L$, and stored the result in a database (see Fig. 1). This database was constructed with a C++ adaptation of the program DIFFRACT from Ph. Lambin, which uses the exact theory developed in [17]. For each tube, we compared the values of θ_1 and the values of D^+, D^- within uncertainties, to the theoretical ones, extracted from the database. We obtained, for each tube, about 10 solutions per diameter range. We then made a simulation of the layer-lines intensity for all the theoretical solutions. Simulations were also performed with a C++ adaptation of DIFFRACT [19]. Before analysing in detail both tubes, it is important to note that, for each tube, only one diameter range (*i.e.* either D^+ or D^- plus uncertainties) is possible. Indeed, a simple eye-checking allows us to eliminate solutions for which the pseudo-periods of the theoretical results do not match, even approximately, the experimental ones. This discrepancy between the experimental data and the theoretical one for a particular diameter range arise from the fact that these pseudo-periods are inversely proportional to $2\pi/D$. This is illustrated in Figure 6 for Tube A and Figure 7 for Tube B, which compares respectively the experimental profiles of $L_{A,3l}$ and $L_{B,-3r}$ with their theoretical counterparts. We can then identify unambiguously tube A to be the outer one and tube B to be the inner one. Let us now discuss the remaining solutions for each tube separately.

– Tube A.
We first calibrate the diffraction pattern with $G_{3,A} = 2\pi/d_{zz}$. Within the described uncertainties, we found 12 solutions. As previously described in Section 3.2.1, due to the curvature effect, $G_{3,A} = 2\pi/d_{zz}\tau$. For all theoretical solutions, it was found that $\tau = 1.0076 \pm 0.1\%$. It is then easy to recalibrate the diffraction pattern taking into account this correction, and we find the calibration to be 5.9791×10^{-3} rd^{-1}Å^{-1} pixel^{-1}. The only remaining errors on the calibration are then due to intrinsic measurement errors and tilt, and these should not exceed 2%.

To find the right solution, we systematically compute different quantities, summarized in Table 1. After the chiral indices, the angles θ_i, the corresponding Bessel functions orders, we give the different ratios between the layer-lines positions, divided by the corresponding experimental values. These quantities do

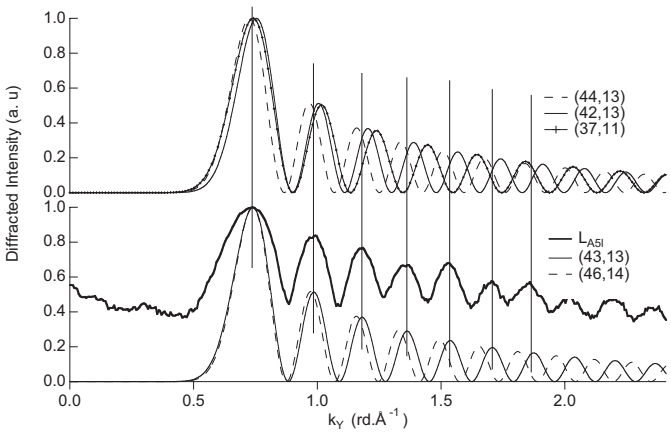

Fig. 6. Experimental and theoretical diffracted intensity for layer-line L_{A-3l}. Bottom panel: Experimental result together with simulation for the (43,13) and the (46,14) tubes, which correspond to the best solutions regarding the layer-line position ratio. By simple visual comparison, the latter has however to be discarded. Top panel: Simulation for (44,13), (42,13) and (37,11). This last solution would be possible only if the A tube would have been the internal one. A simple visual comparison of the distances between maxima between this simulation and the experimental data is enough to discard the possibility of tube A being the inner one.

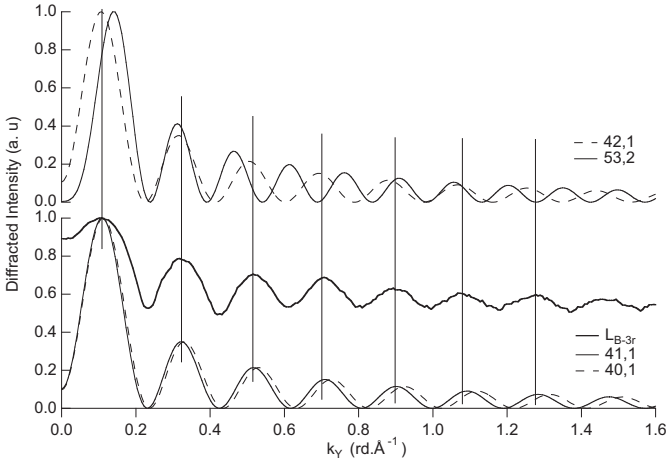

Fig. 7. Experimental and theoretical diffracted intensity for layer-line L_{B-3r}. Bottom panel: Experimental result together with simulation for the (41,1) and the (40,1) tube. Although the two solutions are visually very close, (41,1) is the best numerically fitting solution. Top panel: Simulation for (42,1) and (53,1). This last solution would be possible only if the B tube would have been the external one. A simple visual comparison of the distances between maxima between this simulation and the experimental data is enough to discard the possibility of the tube B being the outer one. The misalignment of the first maxima of this simulation with respect to that of the experimental one is related to the fact that the first Bessel function contributing to the intensity is of order 2, while that of the experimental one is of order 1.

Table 1. Some of the possible structures for tube A. Only the best and worst solutions are displayed. The chiral indices are given, together with the radius and helicity. For each of the 3 first layer-lines, characteristic angles, first contributing Bessel function order, normalized ratios as well as dilatation are given. The (43,13) and (46,14) solution offer the best agreement with experiment considering the layer position ratios. (46,14) should be discarded because of the strong dilation needed to fit the intensity on the layers. Angles are given in units of degrees and radii in units of Å, and layer position ratios are normalized to their experimental counterparts.

(l,m)	R	φ	θ_1 (φ_{app})	θ_2	θ_3	n_1	n_2	n_3	k_{z_2}/k_{z_1}	k_{z_3}/k_{z_1}	k_{z_3}/k_{z_2}	a_1	a_2	a_3
41 13	19.4	13.3	15.9 (14.1)	41.5	74.8	–54	41	–13	0.966	0.979	1.01	1.0522	1.0351	1.0442
42 13	19.8	13.1	16.1 (13.9)	41.3	75.1	–55	42	–13	0.985	0.993	1.008	1.0108	1.0205	1.0243
43 13	20.2	12.8	16.4 (13.6)	41.1	75.4	–56	43	–13	1.004	1.0069	1.0023	1.0156	1.0076	1.0042
44 13	20.5	12.6	16.6 (13.4)	40.8	75.7	–57	44	–13	1.023	1.02	0.998	0.99082	0.99432	0.98463
45 13	20.9	12.3	16.9 (13.1)	40.6	75.9	–58	45	–13	1.04	1.03	0.991	0.98422	0.98199	0.96705
46 14	21.6	12.9	16.3 (13.7)	41.2	75.4	–60	46	–14	0.999	1.00312	1.0039	0.96346	0.95792	0.94975
48 14	22.4	12.4	16.8 (13.2)	40.8	75.9	–62	48	–14	1.03	1.03	0.994	0.93779	0.93915	0.91815

not depend on the calibration, nor on the tilting angle nor on a potential twist of the nanotube. Moreover, because the $k_{z,i}$ are experimentally known with the precision of one pixel, this is the most precise criterion to discriminate between solutions. The best solutions, *i.e.* those for which $\frac{k_{z,i}/k_{z,j}|_{exp}}{k_{z,i}/k_{z,j}|_{theo}}$ are the nearest to 1 for all pairs of layer-lines (i,j) are $(43,13)$ and $(46,14)$. $(42,12)$ is the next best solution. However, contrary to the first two ones $\frac{k_{z,i}/k_{z,j}|_{exp}}{k_{z,i}/k_{z,j}|_{theo}}$ has a variation of 2.2% for different values of (i,j). For (43,13) and (46,14) this variation drops down to 0.4%. Such an error could be explained by apparatus imperfection (effect of spherical aberration of the imaging lens on the diffraction pattern, remaining astigmatism in the intermediate lens...). This is not the case for a 2.2% variation, and thus $(42,12)$ should be discarded.

However, two solutions still remain. By fitting the experimental diffraction pattern with the simulations, one can easily disentangle them. Our goal is to fit the positions of the maxima on a given layer, rather than to fit exactly the diffracted intensity. This latter task would require taking into account more parameters, in particular the broadening of the diffracted intensity by thermal excitation and by non-elastic losses. We thus fitted the experimental intensity $I_{i,exp}(k_y)$ with the following trial function $A_i I_{i,L,M}(a_i k_y + c_i) + d_i$. $I_{i,L,M}$ is the theoretical intensity for layer i for tube (L,M), and $\{A_i, a_i, c_i, d_i\}$ are some fitting coefficients. The important parameter is a_i, which gives the dilatation needed to adjust the theoretical profile to the experimental one. a_i should be as close as possible to 1. Deviation from this value could be explained by the remaining 2% error in the calibration. Theoretical solutions for which $a_i < 0.98$ or $a_i > 1.02$ should then be discarded. Such a deviation means that the radius is too big, or too small to fit the data. We tried different models for the trial function, including convolution by a Gaussian function and removal of the background with different models, and we checked that the value of a_i was not affected by the particular model or a particular choice of the fitting interval. The last three columns of the Table 1 give the values of a_i. It is obvious that the solution $(46,14)$ should be discarded: the radius is too big. As for the preceding analysis on the layer ratio, $(43,13)$ is also the best solution regarding this last criterion, together with the solution (44,13). This latter nanotube was discarded due to the preceding criterion based on the layer-line position ratios. Note that the solution $(42,12)$ gives rise to a_i values too large to fit the data.

– Tube B.
We applied the same procedure to the tube B. In this case, we directly calibrated the diffracted pattern with the $k_{z,3}$ distance, which should be nearly equal to $2\pi/d_{cc}$, because tube B has a nearly zigzag form. The resulting calibration is 5.99705×10^{-3} rd^{-1} Å^{-1}. By comparison with the database, we found 7 solutions. For all these solutions $k_{z,3} = 1$ within 0.01 %. Thus, no re-calibration is needed, contrary to the case of Tube A. Table 2 gives the result of the analysis on tube B. It is worth noting that this time, it is almost impossible to disentangle the different solutions with the layer-line position ratio, which are all equals to 1 one to within 0.2%! Note for consistency that the computed ratios for solutions for which tube B would have been the external one are in disagreement with the experimental ones.

Comparing the a_i coefficients in Table 2 is sufficient to discard all solutions but $(41,1)$. $(40,1)$ and $(42,1)$ are the two next best solutions, but their a_i coefficients are too large to fit the data. Compared to the tube B, the selection criterion based on a_i is much more straightforward, and the a_i values are more invariant on i for a given tube.

From this analysis, the result is that $(41,1)@(43,13)$ is the only solution to index the experimental tube structure. For that determination to be true, it was guessed that $\Gamma < 6°$. This is in total agreement with the imaging of fringes perpendicular to the tube axis in the image in Figure 2. They can be attributed to the zigzag chains of tube B, with

Table 2. Some of the possible structures for tube B. See Table 1 for details. Note that the layer ratios are all very close and cannot help to distinguish between solutions. On the other hand, the dilatation factors unambiguously allow to distinguish (41,1). Angles are given in units of degrees and radii in units of Å, and layer position ratios are normalized to their experimental counterparts.

(l,m)	Radius	φ	θ_1 (φ_{app})	θ_2	θ_3	n_1	n_2	n_3	k_{z_2}/k_{z_1}	k_{z_3}/k_{z_1}	k_{z_3}/k_{z_2}	a_1	a_2	a_3
39 1	15.7	1.26	27.2 (2.76)	29.6	87.7	–40	39	–1	0.995	0.996	1	1.035	1.048	1.05
40 1	16.1	1.22	27.3 (2.71)	29.6	87.8	–41	40	–1	0.997	0.997	1	1.016	1.0193	1.023
41 1	16.5	1.2	27.3 (2.66)	29.6	87.8	–42	41	–1	0.999	0.998	0.999	1.0006	1.009	0.998
42 1	16.9	1.17	27.4 (2.61)	29.6	87.9	–43	42	–1	1	0.999	0.999	0.99007	0.99455	0.978
43 1	17.3	1.14	27.4 (2.57)	29.6	88	–44	43	–1	1	1	0.998	0.97	0.97	0.954
44 1	17.7	1.11	27.5 (2.52)	29.6	88	–45	44	–1	1	1	0.997	0.954	0.956	0.934
45 1	18.1	1.09	27.5 (2.48)	29.6	88	–46	45	–1	1.01	1	0.996	0.94	0.94	0.913

Table 3. Some of the possible structures for TubeB@TubeA. a is the dilatation coefficient.

(l,m) @(l,m)	a
(40,1) @(42,13)	1.0251
(41,1) @(43,13)	1.00418
(42,1) @(44,13)	0.9843
(43,1) @(45,13)	0.96713

$\Gamma = \varphi_B \pm 5°$ [6]. Let us now end coherently our analysis with an analysis of layer L_0, where the contributions of the two tubes interfere.

3.2.5 Comparison to solutions extracted from L0 layer

The calibrations of tube A and B differ only by $\sim 0.3\%$. Because the two calibrations were done totally independently, this validates our calibration procedure. With this new calibration, we re-compute the values of $\overline{D}$ and δD, as well as the corresponding uncertainties, of the order of $\pm 6\%$ and $\pm 4\%$ respectively). By comparison with the database, we searched for the pairs of tubes corresponding to such mean diameters and intertube distance, given the measured θ_1's, as already described in [11]. 7 solutions were found (four of them are summarized in Tab. 3). Among them, we retrieve independently the solutions (41,1)@(43,13), (40,1)@(42,13) and (42,1)@(44,13), for which the inner and outer tubes were among the best solutions in the previous analysis. The top of Figure 8 displays these 3 solutions over a short range of wave vectors. Almost all solutions can be discarded by eye (see the solution (42,1)@(44,13) for example). Also, we apply the same fitting procedure to L_0 as for the other layers. The dilatation factor a is given for some solutions in Table 3. The best fitting solution, plotted on a large wave vector scale in Figure 8, is (41,1)@(43,13). We thus found independently, the same solution as for the separate tube A and tube B analysis. Note that we certainly overestimated the errors on $\overline{D}$ and δD: (41,1)@(43,13) is the only remaining solution extracted from the database when decreasing arbitrarily the uncertainties down to 3.5% for $\overline{D}$ and down to 2% for δD. This means that a simple comparison of the experimental θ_1 and $\overline{D}$ and δD with their theoretical counterparts could be enough in case of high signal to noise ratio, provided the calibration procedure is done as described in the present study.

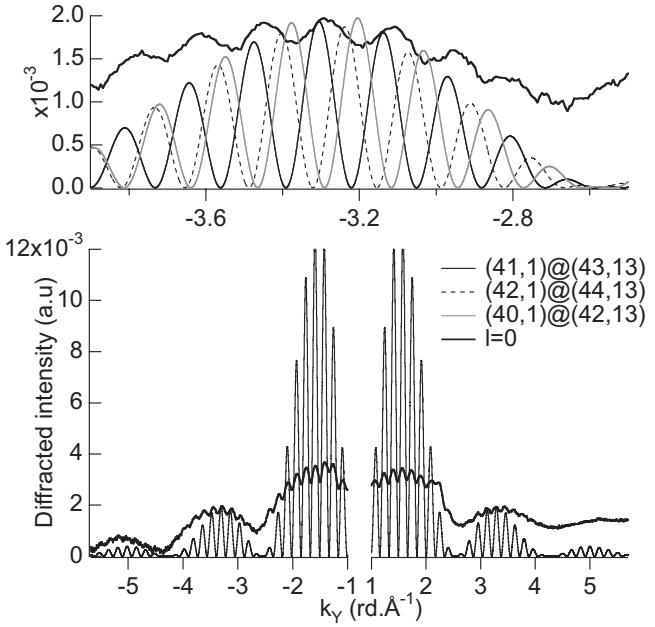

Fig. 8. Experimental and theoretical diffracted intensity for layer-line $l = 0$. The calibration of the abscissa is done with the same calibration as used for Tube B. Bottom panel: Experimental result together with simulation of the best solution (41,1)@(43,13) tube. Top panel: Experimental result and simulation with the three possible solutions (41,1)@(43,13), (40,1)@(42,13) and (42,1)@(44,13) over a short range of wave vectors. (41,1)@(43,13) fits the best.

4 Discussion

In the preceding section, we showed how to determine the chiral indices of both nanotubes inside a DWNT. Let us now discuss the hypothesis beyond this affirmation. We will then discuss the advantage of the above methods, and finally its limitations and drawbacks.

4.1 Underlying hypothesis

The hypotheses underlying this analysis are very weak. The nanotube structure only needs to be well modelised by a sheet of graphene wrapped onto a cylinder. This means that the different relations between distances are true (the relation between the zigzag distance to the carbon-carbon distance, $d_{zz} = 1.5d_{cc}$ for example). With this in mind, the hexagons of the honeycomb lattice must not be distorted (in real space, of course) or, in other words, d_{cc} must be constant over the whole nanotube. Also, a flattening of the nanotube due to interaction with the substrate [20] is unlikely to happen for a suspended structure. Note that these hypothesis is however underlying all forms of chiral indices determination, either implicitly (if the determination is based upon electronic structure [8,10]) or explicitly (real-space determination by STM [4] or phase-reconstructed HR (PRHR) [6]). Also, the presented technique is robust with respect to a possible twist of the nanotube. Indeed, the layer position ratios are not dependent on a twist (because a twist is in an homothetic operation along the tube axis), and we saw that in tubes like tube A, a selection of solutions based on these ratii is very robust.

The interest of the described method is that it is almost independent of any fitting parameter. Because the calibration of the diffraction pattern is done directly on itself, the chiral indices can be extracted without knowing the value of d_{cc}. This is different from the above-mentioned techniques. The real-space methods do depend of the knowledge of d_{cc}, although auto-calibration could be in principle be done in PRHR. In the case of techniques, like STS or Raman spectroscopy, where the determination of the chiral indices depends upon a band-structure model, the analysis depends also on a second parameter, namely the value of the hopping integral γ_0. It is worth noting that, if the value of γ_0 is consistent within a technique, there's no agreement between the fitted values of γ_0 between the 2 kinds of experiments (STS and Raman), although the same tight-binding model is used to fit the data. This is not the case here.

However, there are some drawbacks in this method. The handness could not be extracted from the diffraction solely. Similarly, for chiral tubes, the absolute shift z_0 or rotating angle ϕ_0 cannot be measured. These two impossibilities are related to the fact that neither the intensity of the equatorial line (Eq. (9)) nor that of the other lines (Eq. (8)) are dependent on σ, z_0 or ϕ_0. The situation would be different for achiral tubes, for which more than one Bessel function, weighted by a phase factor generally depending on σ, z_0 or ϕ_0, contribute to the diffracted intensity. The handness could however be measured in the general case, provided we could access the HR image of the tube, and we could experimentally change Γ. Indeed, when the zigzag chains are approximatively parallel to the electron beam, the contrast becomes periodic along the direction of the tube axis, on one of the two sides (see Fig. 2). The knowledge of the sign (unknown in the present experiment) of the tilt would allow a retrieval of the handness. Of course, the accuracy in determining the chiral indices, reflected for example in the precision achievable in determining the layer-line position ratii, comes from the fact that the diffracted signal comes from a wide region (about 500 nm) of the nanotube, *i.e.*, the diffraction is non-local. No local information can be then gained. Nevertheless, local information on defects, for example, can be obtained by HR on the very same NT.

4.2 Domain of applicability of the method

Finally, the domain of applicability of the present method can be extended to other types of nanotubes or group of nanotubes. It is of course possible to apply such a technique to SWNT. Given a radius estimated at 12% and a measured helicity, we proved it by analysing separately the two tubes in Section 3.2.4. However, in this case, an estimation of the radius is not as straightforward as for the DWNT, because the intensity on the equatorial line falls experimentally to zero before it is possible to conveniently approximate a Bessel function by a cosine. In that case, the radius could be first estimated by HR, for example, and its value crosschecked by fitting the equatorial line with the appropriate law [12]. One of the advantages of the electron diffraction technique is that it allows, thanks to its precision, a deduction of chiral indices even for large radius (*i.e.*, up to 40Å) (contrary to what is possible with Raman spectroscopy, for example). Also, it is not restricted to surface analysis (like STM/STS) or dependent on the influence on the tube by its environment, thus can probe MWNT and ropes. Concerning MWNT, there's no reason why we could not extend our method to them. Thanks to the diameter differences between constituant tubes, each layer-line could be easily attributed solely to one tube, provided the tubes periods along the axis are not commensurate. This is possible in practice only when the number of walls is small. Then, the analysis of the non-equatorial layers follows exactly Sections 3.2.2, 3.2.3 and 3.2.4. Crosschecking of Section 3.2.5 would be possible, but would become more difficult with an increasing number of tubes. Concerning ropes, the problem is more intricate. Indeed, they consist usually of a huge set of SWNT with a distribution of diameters and helicities. More importantly, they can be highly disordered, having different tube axis directions or being twisted with respect to each other [15]. However, ropes of tubes with a unique helicity and diameters were recently formed and studied by electron diffraction [14]. Their equatorial line and apparent helicities were analysed. The present method and in particular the analysis of the non-equatorial line could be used. The determination of chiral indices of nanotube of other species, like BN or WS_2 could also in principle be studied, because the underlying theory can be easily adapted to all kinds of honeycombs structure [17].

5 Conclusion

We have presented a detailed method, exemplified by one example, for determining the chiral indices of DWNT. This method relies on the semi-quantitative analysis of

the whole diffraction pattern of a nanotube. Simulation of the diffracted intensity and extensive comparison with theory is needed. This method is accurate enough to unambiguously give the chiral indices of SWNT's of radii on the order of 20 Å, given overestimated initial uncertainties of the order of $\pm 12\%$ for the diameters, and $\pm 0.6°$ for the (apparent) helicities. We crosschecked this affirmation by analysing both the regions of the diffraction pattern of a DWNT where its two constituant tubes contribute independently and the regions where their contributions interfere. Using this method, SWNT of large diameter could be studied. The chiral indices of each tube constituting a MWNT are also possible. Contrary to spectroscopic methods, which rely on some empirical parameter, we show that the present method does not rely on any free parameters. In particular, the knowledge of the exact value of the carbon-carbon bond length d_{cc} is not needed. This method could be systematically used in the future to combine physical measurements with structural determination of chiral indices on nanotubes, as previously shown in favourable cases [11].

Ph. Lambin and L. Henrard provided us with the FORTRAN code of DIFFRACT and many explanations on it. It's a pleasure to thanks L. Henrard, Ph. Lambin, A. Lucas, J-F. Colomer and P. Launois for the constant discussions about nanotubes diffraction. We thank O. Stéphan and L. Henrard for their careful reading of the manuscript and their suggestions to improve it. We are grateful to Y. Saito for providing us with the samples, and T. Saito and Y. Sasaki for their assistance in using IP.

References

1. S. Iijima, Nature **354**, 56 (1991)
2. S. Iijima, T. Ichihashi, Nature **363**, 603 (1993)
3. N. Hamada, S.I. Sawada, A. Oshiyama, Phys. Rev. Lett. **68**, 1579 (1992)
4. J.W.G. Wildoer, L.C. Venema, A.G. Rinzler, R.E. Smalley, C. Dekker, Nature **391**, 59 (1998)
5. T.W. Odom, J.-L. Huang, P. Kim, C.M. Lieber, Nature **391**, 62 (1998)
6. S. Friedrichs, J. Sloan, M.L.H. Green, J.L. Hutchison, R.R. Meyer, A.I. Kirkland, Phys. Rev. B **64**, 045406 (2001)
7. L.-C. Qin (1994) in *Progress in Transmission Electron Microscopy 2*, Applications in Materials Science, Springer Series in Surface Sciences, Vol. 39, edited by X.F. Zhang, Z. Zhang (Springer-Verlag / TUP, 2001), pp.73–104
8. V. Meunier, Ph. Lambin Phys. Rev. Lett. **81**, 5588 (1998)
9. Philip Kim, Teri W. Odom, Jin-Lin Huang, Charles M. Lieber, Phys. Rev. Lett. **82**, 1225 (1999)
10. A. Jorio, R. Saito, J.H. Hafner, C.M. Lieber, G. Dresselhaus, M.S. Dresselhaus, Phys. Rev. Lett. **86**, 1118 (2001)
11. M. Kociak, K. Suenaga, K. Hirahara, Y. Saito, T. Nakahira, S. Iijima, Phys. Rev. Lett. **89**, 155501 (2002)
12. M. Gao, J.M. Zuo, R.D. Twesten, I. Petrov, L.A. Nagahara, R. Zhang to be published in Appl. Phys. Lett. (2003)
13. S. Amelinckx, A. Lucas, P. Lambin Rep. Prog. Phys. **62**, 1471 (1992)
14. J.-F. Colomer, L. Henrard, Ph. Lambin, G. Van Tendeloo Phys. Rev. B **64**, 125425 (2001)
15. L. Henrard, A. Loiseau, C. Journet, P. Bernier, Eur. Phys. J. B **13**, 601 (2001)
16. K. Hirahara, S. Bandow, M. Kociak, M. Yudasaka, T. Nakahira, K. Itoh, Y. Saito, S. Iijima (unpublished)
17. Ph. Lambin, A.A. Lucas, Phys. Rev. B **56**, 3571 (1997)
18. R. Saito, G. Dresselhaus, M. S. Dresselhaus, *Physical properties of carbon nanotubes* (Imperial College Press 1998), Chap. 4
19. The source code for the programms SelectionRules, LayerGen, NTDataBaseWriter and NTDataBaseReader, as well as the database of Figure 1 are available on request
20. T. Hertel, R.E. Walkup, P. Avouris, Phys. Rev. B **58**, 13870 (1998)